ACS APPLIED MATERIALS & INTERFACES

www.acsami.org

Research Article

A Magnetically Responsive Flexible Thermal Switch for Reversible Thermal Regulation

Yuxia Dong, Xudong Zhang,* Bin Li, Guanghao Sang, and Bingyang Cao*

Cite This: *ACS Appl. Mater. Interfaces* 2026, 18, 15345−15354

Read Online

ACCESS | Metrics & More | Article Recommendations | Supporting Information

ABSTRACT: Dynamic regulation of thermal conductivity is fundamental to smart thermal management and energy conservation. As a key component, a thermal switch enables smart thermal regulation by reversibly toggling thermal conductivity between high and low states. However, achieving flexible and continuous thermal switches remains a significant challenge. Here, a magnetically responsive flexible thermal switch composed of magnetic liquid metal, graphene films, and polydimethylsiloxane is developed. The flexible thermal switch exhibits a reversible and dynamic variation in thermal conductivity between 0.261 and 3.426 $W \cdot m^{-1} \cdot K^{-1}$, with a thermal switching ratio of 13.1. At different heat flux densities, the temperature difference between device and environment in the "on" state of flexible thermal switch is reduced by approximately 57.9% compared with that in the "off" state. Furthermore, a flexible thermal switch reduces the temperature deviation of a foldable smartphone heat source by 10.2%. It demonstrates excellent temperature regulation capability that can be applied to planar, curved, and wearable devices. This work provides promising opportunities for smart thermal management in curved and wearable devices such as soft robotics and foldable smartphones.

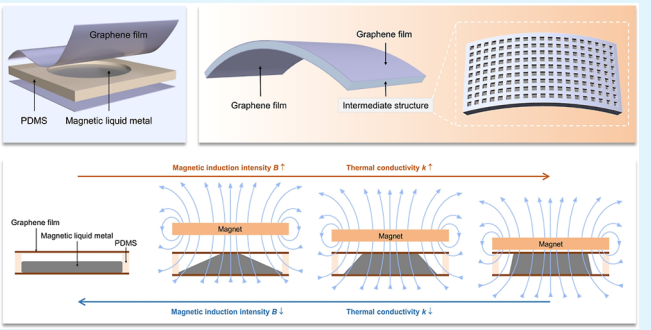

KEYWORDS: *flexible thermal switch, high switching ratio, reversible thermal regulation, liquid metal, smart thermal management*

1. INTRODUCTION

Heat transfer generally occurs in all energy transport and conversion processes. Dynamic and controllable thermal transport can enable energy conservation[1,2] and improve operating efficiency of electronic devices.[3,4] It is reported that building envelopes with variable thermal conductance can achieve energy savings of 7−42% in different cities across the United States.[5] Most devices, such as electronic chips,[6] power batteries,[7] and spacecraft,[8] can only operate within a specific temperature range. Hence, changes in ambient temperature or fluctuations in device power can cause thermal management failures, resulting in performance degradation and even device damage. Therefore, there is a growing demand for smart thermal control components with tunable thermal conductivity.[9] Smart thermal control components can also be employed as thermal metamaterials[10] and in the design of thermal computers.[11]

Thermal switches are smart thermal control components that can switch between "on" and "off" states,[12] making them effective tools for heat flow regulation. The thermal switching ratio (r) is the most critical performance parameter of thermal switches, and it is defined as the ratio of thermal conductivity in "on" and "off" states.[13] Numerous studies have been conducted on thermal switches, which are classified based on their regulation mechanisms,[13] including electric field,[14,15] magnetic field,[16−18] light,[19] phase change,[20−22] and mechanical contact,[23,24] as shown in Figure 1d and Table S1. However, most existing thermal switches lack flexibility. With the rapid development of flexible electronics,[25] soft robotics,[26] wearable devices,[27] foldable smartphones,[28] and cylindrical batteries,[29] conventional rigid thermal switches can no longer satisfy thermal management requirement of multidimensional and flexible devices. Flexible thermal switches not only function effectively in planar devices but also maintain stable and controllable thermal regulation in multidimensional devices. However, achieving flexible thermal switches remains a significant challenge, imposing a stricter requirement on both material selection and structural design.

Flexible thermal switches need to be adaptable to curved surfaces, which requires a flexible substrate and a smart responsive medium. Liquid metal, characterized by high thermal conductivity and fluidity,[30] is a particularly promising candidate for fabricating flexible thermal switches.[31] A limited

Received: December 17, 2025
Revised: February 6, 2026
Accepted: March 3, 2026
Published: March 6, 2026

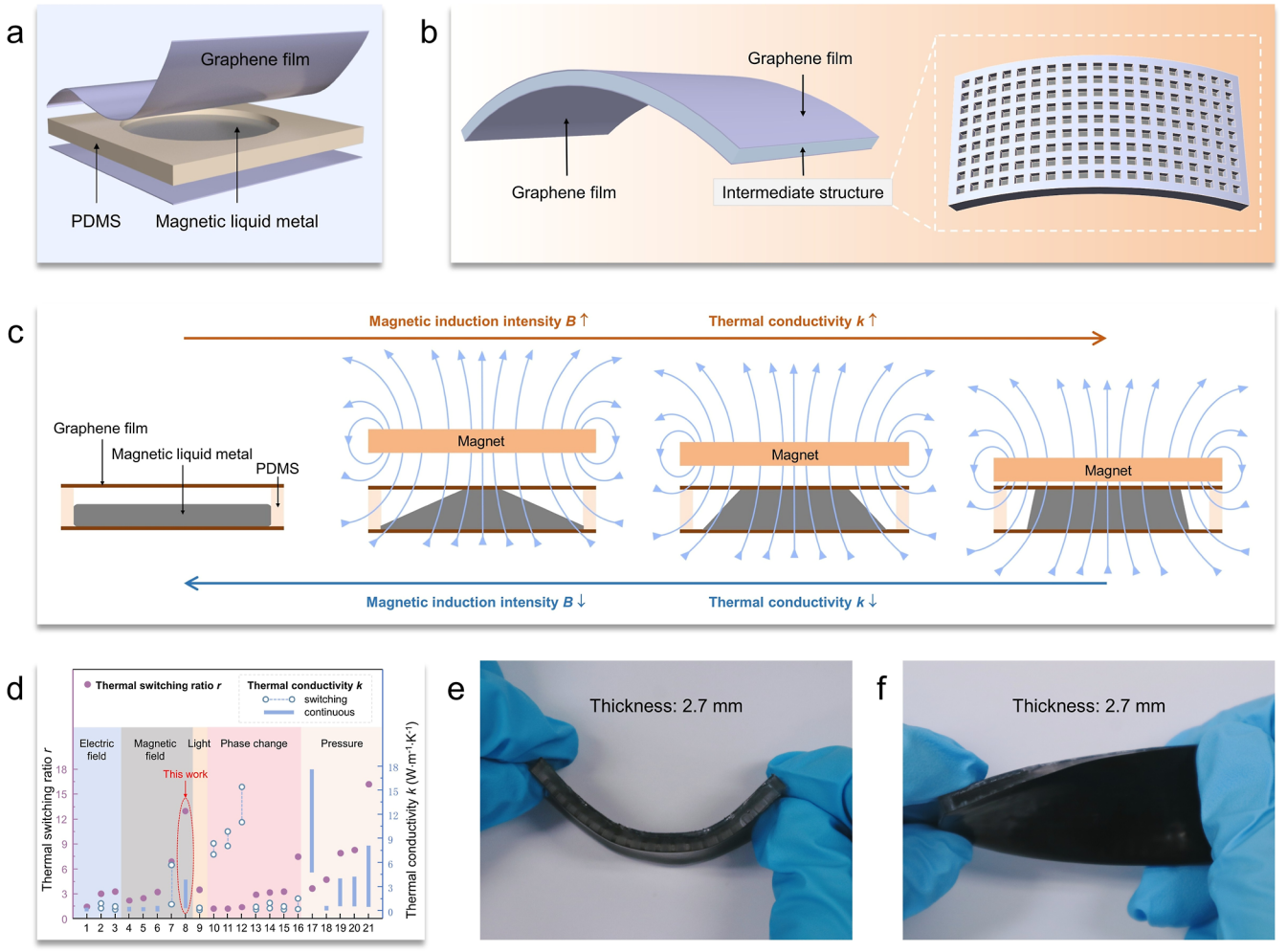

Figure 1. Overview of the flexible thermal switch. (a) Schematic of the simple structure (Structure-A) for experimental characterization. (b) Schematic of the applicable structure (Structure-B) designed for thermal management of curved heat sources. (c) Operating principle of the flexible thermal switch: the heat conduction pathway expands as the magnetic induction intensity increases, causing an improvement in thermal conductivity. (d) Performance comparison of thermal switches with different control mechanisms, where the *x*-axis corresponds to the numbers listed in Table S1. (e) Bending characteristics and (f) twisting characteristics of the flexible thermal switch with a thickness of 2.7 mm.

number of studies have applied liquid metals to the fabrication of flexible thermal switches. Yao et al.[32] introduced a liquid metal network into an elastomer foam and attained a thermal switching ratio of 8.3 under 60% mechanical compression. Zhao et al.[33] also developed a liquid metal shape memory foam and achieved a thermal switching ratio of 4.71 through compression. Yu et al.[24] prepared a superstretchable liquid metal foamed elastomer composite, and obtained a thermal switching ratio of 3.7 along the stretching direction. Current research mainly focuses on mechanical compression and stretching methods, which have risks of liquid metal leakage and inconvenient displacement. By contrast, flexible thermal switches regulated by magnetic field offer significant advantages, such as fast response, flexible operation, and simple structures.[34,35] Magnetic liquid metal is composed of magnetic particles and liquid metal[36] and exhibits large deformability, high thermal conductivity, excellent fluidity, and magnetism.[37,38] These combined properties make it a promising candidate for a magnetically responsive and flexible thermal switch.

In this work, a flexible thermal switch consisting of magnetic liquid metal, graphene films, and poly(dimethylsiloxane) (PDMS) has been developed to achieve a reversible regulation of thermal conductivity under magnetic fields (Figure 1). Two structures based on the same working principle are designed: a simple structure for experimental characterization (Structure-A) and an applicable structure for thermal management of curved heat sources (Structure-B). The applied magnetic field can modulate the heat conduction pathways formed by magnetic liquid metal, thereby regulating thermal conductivity of the flexible thermal switch. This flexible thermal switch enables a continuous adjustment of the thermal conductivity from 0.261 to 3.426 $W \cdot m^{-1} \cdot K^{-1}$, achieving a high thermal switching ratio of 13.1. As shown in Figure 1d and Table S1, the flexible thermal switch presented in this work exhibits a high thermal switching ratio compared with previously reported noncontact thermal switches. The excellent temperature regulation capability of the flexible thermal switch was experimentally demonstrated. The flexible thermal switch exhibits tunable thermal conductivity and flexibility, enabling smart thermal management of both planar and curved heat sources. Notably, it reduced the temperature deviation of a foldable smartphone heat source by 10.2%, highlighting its potential for flexible thermal management. The flexible thermal switch shows great potential for smart thermal management in

https://doi.org/10.1021/acsami.5c25437
ACS Appl. Mater. Interfaces 2026, 18, 15345−15354

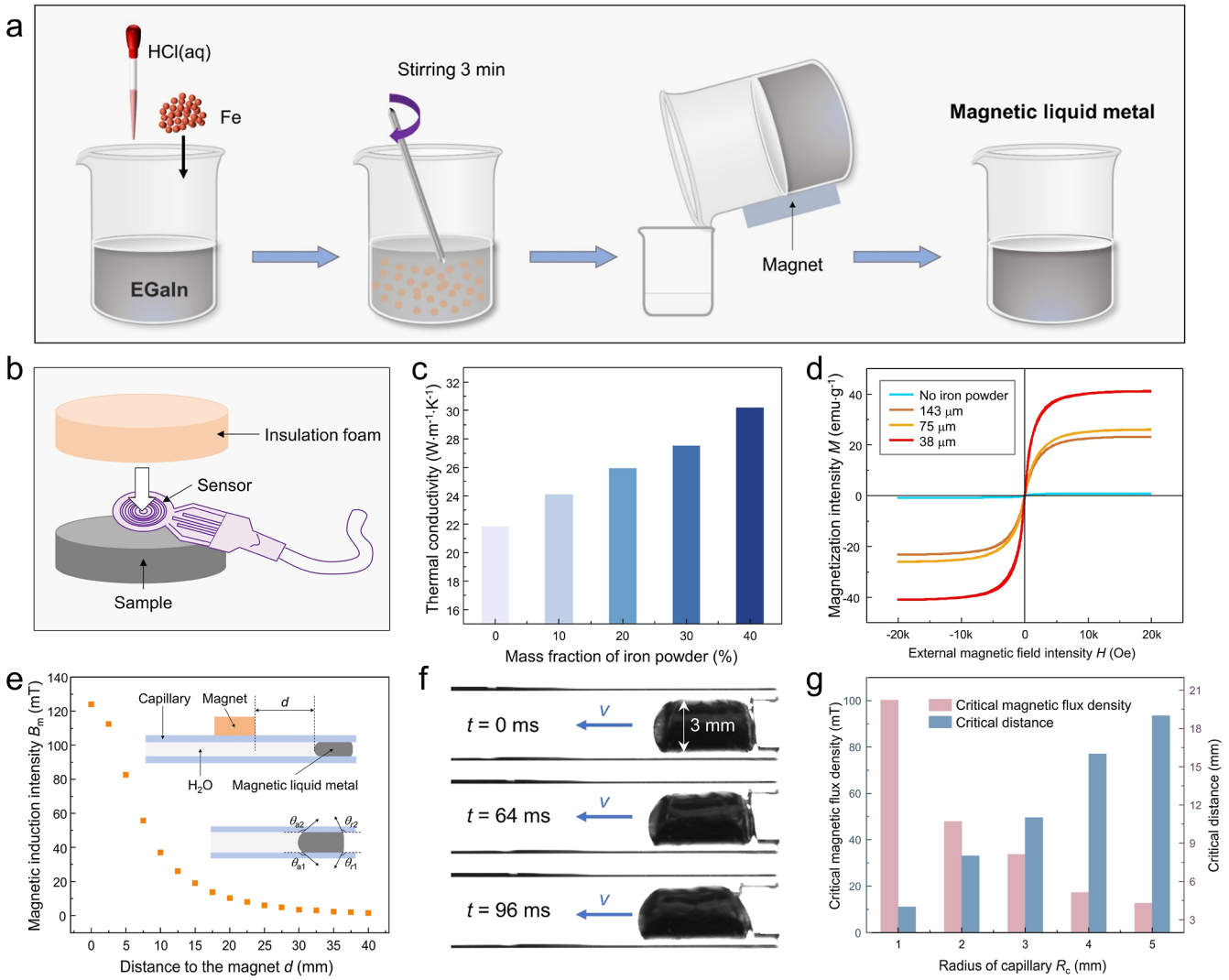

Figure 2. Preparation and properties of magnetic liquid metal. (a) Preparation process of magnetic liquid metal. (b) Measurement of thermal conductivity of magnetic liquid metal by the transient plane source method. (c) Variation in the thermal conductivity of magnetic liquid metal with iron powder mass fraction (particle size: 38 μm). (d) Hysteresis loops of magnetic liquid metal with different iron powder particle sizes (mass fraction: 20%). (e) Magnetic induction intensities at various positions relative to the permanent magnet, along with the schematic representation of the motion experiment of magnetic liquid metal in a capillary. (f) Variation in contact angle at the onset of magnetic liquid metal motion. (g) Relationship between the critical magnetic induction intensity and the capillary radius, along with that between the critical distance and the capillary radius.

wearable electronics, foldable smartphones, cylindrical batteries, and spacecraft.

2. RESULTS AND DISCUSSION

2.1. Preparation and Properties of Magnetic Liquid Metal

Figure 2a illustrates the preparation process of the magnetic liquid metal. Hydrochloric acid removed the oxide layer on the surface of iron powder and eutectic gallium indium (EGaIn), enabling direct contact between them. According to the endocytosis theory of liquid metal, endocytosis readily occurs when the contact angle is less than 90°.[39] The wetting angle between Fe and EGaIn is approximately 32°,[40] facilitating the dissolution of iron powder into EGaIn. The galvanic cell reaction between Ga and Fe prevented the iron powder from being corroded by hydrochloric acid, thereby preserving its magnetic properties.[37,41] The scanning electron microscopy (SEM) image of the magnetic liquid metal is presented in Figure S1.

The thermal conductivity of the magnetic liquid metal was measured using the transient plane source method (Hot Disk TPS 2500 S). The magnetic liquid metal was placed in a container with a diameter of 30 mm and a height of 15 mm (Figure 2b). A 5501 probe was positioned above the magnetic liquid metal with thermal insulation foam placed on top and pressed tightly. The thermal conductivity of magnetic liquid metal was measured by using the single-sided method. Figure 2c reveals that the thermal conductivity of magnetic liquid metal gradually increases with the increasing mass fraction of iron powder at a constant iron particle size, which can be attributed to the higher thermal conductivity of iron particles compared with that of EGaIn. However, increasing the iron powder mass fraction reduced the fluidity of the liquid metal. The magnetic liquid metal containing 20 wt % iron powder provides an enhancement in thermal conductivity while maintaining good fluidity. In the absence of a magnetic field, iron powder particles are randomly dispersed within EGaIn,

https://doi.org/10.1021/acsami.5c25437
ACS Appl. Mater. Interfaces 2026, 18, 15345−15354

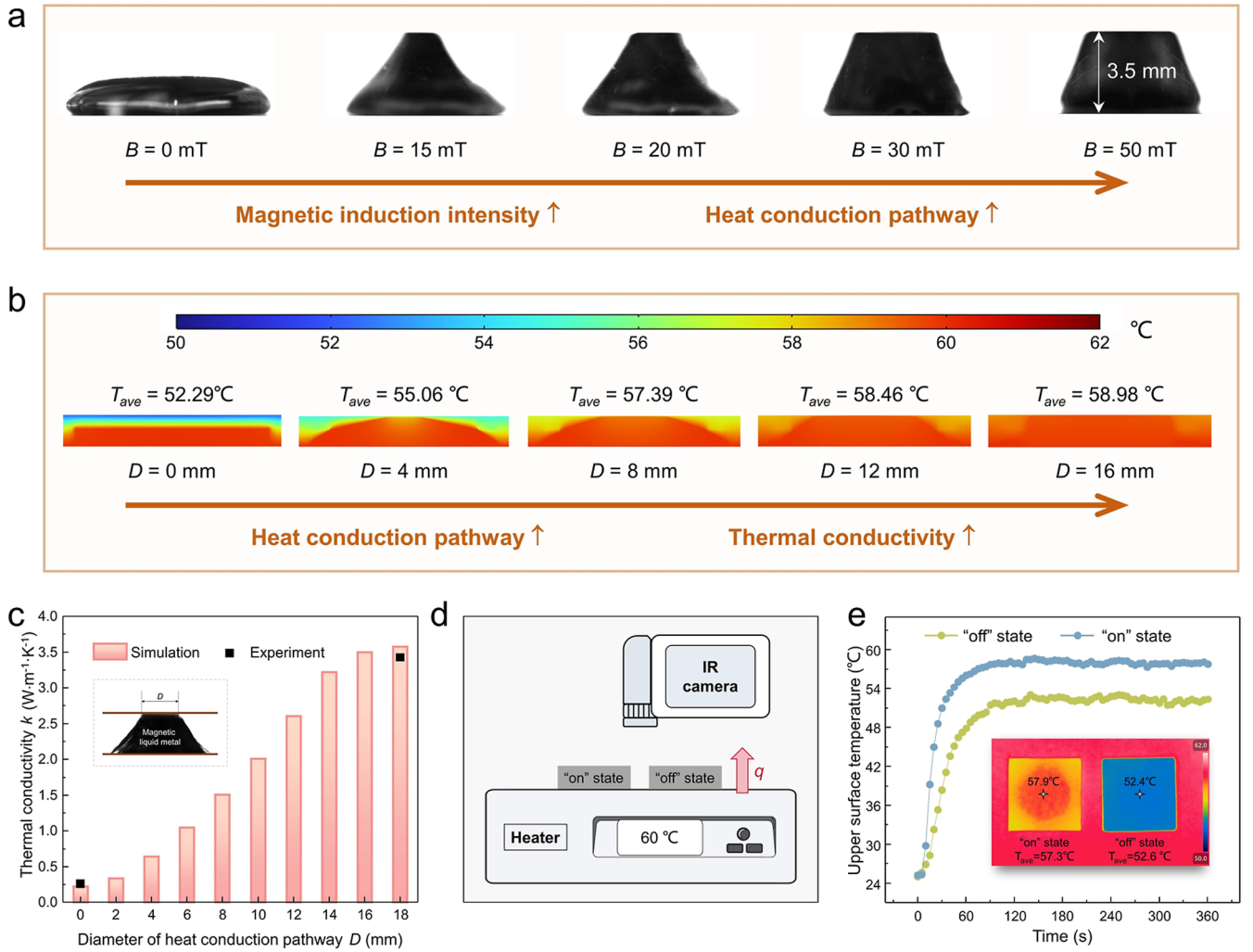

Figure 3. Thermal performance of the flexible thermal switch. (a) Relationship between heat conduction pathway and magnetic induction intensity. (b) Simulated temperature distribution along the central longitudinal section of the flexible thermal switch under different heat conduction pathways. (c) Relationship between the thermal conductivity of flexible thermal switch and heat conduction pathway. (d) Schematic diagram of the experimental setup for measuring temperature rise speed and steady-state temperature distribution. (e) Variation of the upper surface temperature of flexible thermal switch over time, and the steady state surface temperature distribution captured by an infrared thermal imager.

resulting in an isotropic thermal conductivity. By contrast, under a magnetic field, iron powder particles are aligned in the direction of the magnetic field, causing anisotropic thermal conductivity[42] (a more detailed discussion is presented in the Supporting Information). Figure 2d presents the hysteresis loops of magnetic liquid metal containing iron powder particles of varying sizes, while maintaining a constant iron powder mass fraction of 20%. Among these particle sizes, the magnetic liquid metal with 38 μm iron particles exhibits the strongest magnetism, which is favorable for reliable magnetic actuation in the thermal switch. The stronger magnetism observed in magnetic liquid metal with smaller iron particles may be attributed to their more uniform dispersion in EGaIn and better interfacial contact. Considering a balance among thermal conductivity, magnetism, and fluidity, the magnetic liquid metal containing 20 wt % iron powder with an average particle size of 38 μm was used in subsequent experiments.

The addition of iron powder imparted magnetism to EGaIn, allowing it to move under a magnetic field. To quantify the movement of the magnetic liquid metal in capillaries of varying diameters, the critical magnetic induction intensity and the critical distance were defined. The critical magnetic induction intensity is the minimum magnetic induction intensity required to move a magnetic liquid metal, and the critical distance is the maximum distance between a permanent magnet and a magnetic liquid metal required to drive a magnetic liquid metal. Figure 2e presents the magnetic induction intensities at different distances from the permanent magnet. Water and a 5 mm long magnetic liquid metal were injected into capillaries. The permanent magnet was slowly moved close to magnetic liquid metal until magnetic liquid metal started moving (Figure 2f and Video S1). It was noticed that a decrease in the capillary radius resulted in an increase in the critical magnetic induction intensity and a reduction in the critical distance (Figure 2g and Table S2). The magnetic liquid metal in capillaries was subjected to magnetic force, frictional resistance, and resistance caused by surface tension. The water film reduced the frictional resistance acting on magnetic liquid metal, making the frictional resistance negligible. The magnetic force can be expressed as[43,44]

$$F_m = \frac{V\chi}{\mu_0} B_m \cdot (\nabla B_m) \quad (1)$$

https://doi.org/10.1021/acsami.5c25437
ACS Appl. Mater. Interfaces 2026, 18, 15345−15354

where V is the volume of magnetic liquid metal, χ is the magnetic susceptibility of magnetic liquid metal, μ_0 is the permeability of vacuum, and B_m is the magnetic induction intensity generated by permanent magnet. The resistance caused by surface tension can be described as[45]

$$F_\sigma = 2\pi R_c \sigma(\cos\theta_r - \cos\theta_a) \quad (2)$$

where σ represents surface tension, R_c is the radius of capillary, and θ_a and θ_r denote the advancing angle and the receding angle, respectively, which can be approximated as $\cos\theta_a \approx (\cos\theta_{a1} + \cos\theta_{a2})/2$ and $\cos\theta_r \approx (\cos\theta_{r1} + \cos\theta_{r2})/2$, respectively. The magnetic liquid metal starts to move when the magnetic force exceeds the resistance caused by the surface tension. According to the critical state equation $F_m = F_\sigma$

$$B_m \cdot (\nabla B_m) = \frac{1}{R_c} \cdot \frac{2\mu_0 \sigma(\cos\theta_r - \cos\theta_a)}{L\chi} \quad (3)$$

The formula indicates that a smaller capillary diameter requires a higher magnetic induction intensity to drive magnetic liquid metal.

2.2. Thermal Performance of the Flexible Thermal Switch

When a permanent magnet is placed above a magnetic liquid metal, it deforms into a bulge. Upon removal of the magnetic field, the magnetic liquid metal returns to its original state due to gravity (Video S2). Based on this property, a flexible thermal switch consisting of magnetic liquid metal, graphene films, and PDMS was designed. Graphene films were selected as the top and bottom encapsulation layers because of their high in-plane thermal conductivity, which facilitates a more uniform temperature distribution on the upper and lower surfaces. The flexible thermal switch exhibits a response time of approximately 0.2 s. Figure 1a shows the schematic of the Structure-A flexible thermal switch, which is used for performance characterization. Under a magnetic field, magnetic liquid metal bulges and contacts the graphene film at the upper end, establishing a heat conduction pathway. In this state, the flexible thermal switch is in the "on" state and exhibits high thermal conductivity. In the absence of magnetic field, the heat conduction pathway is disconnected due to gravity, and the flexible thermal switch reverts to the "off" state with low thermal conductivity. The thermal conductivity of the flexible thermal switch was measured by the steady-state method (Longwin LW-9389MD), and the experimental details are provided in the Supporting Information. As the steady-state testing process requires pressure and PDMS has limited mechanical strength, a transparent resin with a thermal conductivity similar to that of PDMS was used as a substitute. The thermal conductivity of the flexible thermal switch is 0.261 $W \cdot m^{-1} \cdot K^{-1}$ in the "off" state and 3.426 $W \cdot m^{-1} \cdot K^{-1}$ in the "on" state, resulting in a thermal switching ratio of 13.1, which is significantly higher than that of other thermal switches based on noncontact regulation mechanisms. The Supporting Information provides the total thermal resistance network of the flexible thermal switch, showing that the overall thermal resistance in the "off" state is significantly higher than that in the "on" state. Unlike static high-thermal-conductivity materials, the flexible thermal switch exhibits tunable thermal conductivity, enabling adaptive temperature regulation under fluctuating thermal loads. Specifically, the thermal conductivity is reduced in low-temperature environments to enhance thermal insulation, while it is increased under high thermal loads to improve heat dissipation.

The flexible thermal switch also enabled continuous modulation of thermal conductivity by adjusting the magnetic induction intensity (B). A high-speed camera was used to capture images of heat conduction pathways formed by magnetic liquid metal under different magnetic induction intensities (Figure 3a), and the results demonstrated that the heat conduction pathway progressively expanded with the increase in magnetic induction intensity. The temperature distribution of the flexible thermal switch under different heat conduction pathways was simulated using finite element method. Models with varying heat conduction pathways were constructed based on the images captured by a high-speed camera (detailed simulation parameters are provided in the Supporting Information). The volume of magnetic liquid metal was kept constant. The heat conduction pathway diameter (D) was defined as the diameter of the contact area between magnetic liquid metal and the upper graphene film, and the larger the D value, the broader the heat conduction pathway. In the simulation, the lower surface temperature of the flexible thermal switch was fixed at 60 °C and the upper surface was subjected to natural convection with air. Figure 3b displays the temperature distribution along the central longitudinal section of the flexible thermal switch under different heat conduction pathways. The upper surface temperature and overall temperature uniformity of flexible thermal switch increased with the expansion of the heat conduction pathway, indicating a gradual improvement in thermal conduction. Furthermore, thermal conductivity of flexible thermal switch under different heat conduction pathways was simulated through finite element method. In the simulation, the upper surface temperature of the sample was maintained at 20 °C; the lower surface heat flux was set to 5000 $W \cdot m^{-2}$; and all other parameters were consistent with those described above. Based on these conditions, thermal conductivity of flexible thermal switch under different heat conduction pathways was calculated. It is evident from Figure 3c that an expansion in the heat conduction pathway led to a notable increase in thermal conductivity of the flexible thermal switch. Therefore, the thermal conductivity of the flexible thermal switch can be continuously tuned by varying magnetic induction intensity, which is attributed to the changes in heat conduction pathways caused by the morphological transformation of magnetic liquid metal under magnetic field.

As shown in Figure 3d, two flexible thermal switches were positioned on a heating stage maintained at 60 °C. One flexible thermal switch was in the "on" state, while the other was in the "off" state. Thermocouples recorded the temperature change of the upper surface over time, and an infrared thermal imager captured the steady-state temperature distribution. Figure 3e demonstrates that the flexible thermal switch in the "on" state heated up more rapidly, indicating a higher thermal diffusivity in comparison to that in the "off" state. As shown in Figure 3e, the center region of the upper surface in the "on" state exhibited a higher temperature, which was attributed to the formation of a heat conduction pathway. The central point temperature in the "on" state was 5.5 °C higher than that in the "off" state. Additionally, the average temperature of the upper surface T_{ave} in the "on" state was 4.7 °C higher than that in the "off" state, further indicating a higher thermal conductivity in the "on" state, consistent with the thermal conductivity test results.

https://doi.org/10.1021/acsami.5c25437
ACS Appl. Mater. Interfaces 2026, 18, 15345−15354

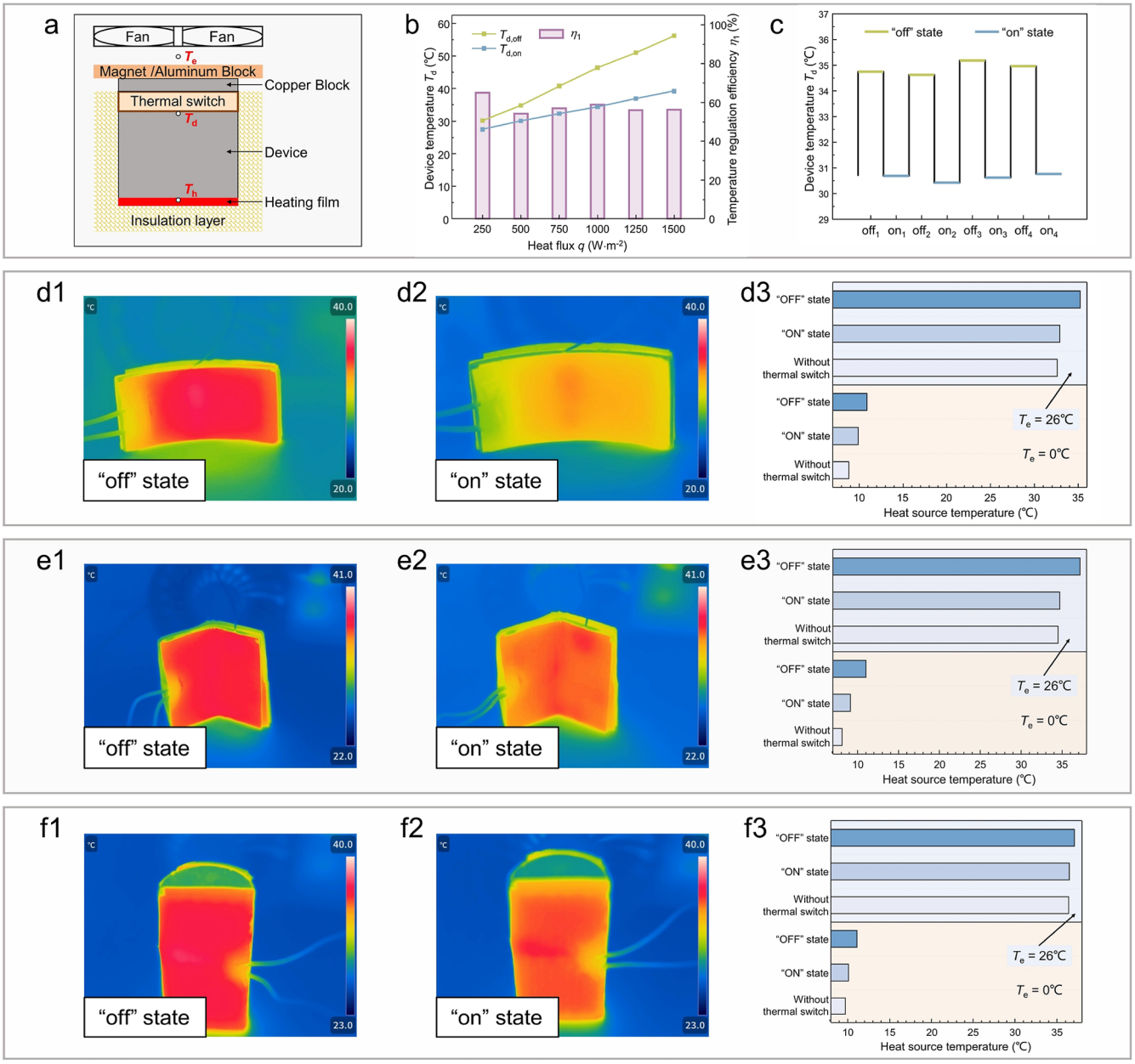

Figure 4. Temperature regulation performance of the flexible thermal switch. (a) Experimental setup for testing temperature regulation ability and reversibility of the flexible thermal switch. (b) Variation of device temperature and temperature regulation efficiency with heat flux. (c) Reversible thermal conductivity regulation of the flexible thermal switch. (d,e) Smart thermal management of different curved heat sources using the flexible thermal switch. Curved monitor: (d1) temperature distribution with the flexible thermal switch in the "off" state at T_e = 26 °C, (d2) temperature distribution with the flexible thermal switch in the "on" state at T_e = 26 °C, and (d3) heat source temperatures under different conditions. Foldable smartphone: (e1) temperature distribution with the flexible thermal switch in the "off" state at T_e = 26 °C, (e2) temperature distribution with the flexible thermal switch in the "on" state at T_e = 26 °C, and (e3) heat source temperatures under different conditions. Cylindrical battery: (f1) temperature distribution with the flexible thermal switch in the "off" state at T_e = 26 °C, (f2) temperature distribution with the flexible thermal switch in the "on" state at T_e = 26 °C, and (f3) heat source temperatures under different conditions.

2.3. Temperature Regulation Performance of the Flexible Thermal Switch

To investigate the temperature regulation performance of the flexible thermal switch, an experimental system was designed to simulate its actual heat dissipation performance. The experimental system consisted of a heating film, a device, and heat dissipation components, which included a cooling fan, a magnet/aluminum block, a copper block, and a flexible thermal switch based on magnetic liquid metal (Figure 4a). A polyimide heating film (25.5 × 25.5 mm^2) served as the heat source, and an aluminum block was placed on the heating film as a device to be dissipated. A copper block was positioned between the flexible thermal switch and the magnet to act as a separator, which prevented the magnetic force from making magnet removal difficult. The magnet and aluminum block, each with a side length of 30 mm, were both employed for comparative analysis. When the magnet was applied, the flexible thermal switch was in the "on" state, whereas when the aluminum block was used, the thermal switch reverted to the "off" state. A cooling fan was located above the system to

https://doi.org/10.1021/acsami.5c25437
ACS Appl. Mater. Interfaces 2026, 18, 15345−15354

enhance the convective heat transfer. To minimize heat loss from the system surface, a foam insulation layer was applied between the system and ambient air. The system temperature was measured by using thermocouples. The temperature between the device and the thermal switch was defined as the device temperature (T_d), and the thermocouple floating in the air measured the environmental temperature (T_e).

The environmental temperature (T_e) was set to 26 °C, and the input heat flux (q) was gradually raised from 250 to 1500 W·m^{-2}. The device temperatures (T_d) of the flexible thermal switch in the "on" and "off" states were measured separately. It is observable from Figure 4b that the device temperature increased gradually with a rise in heat flux. Here, the temperature regulation efficiency (η_1) is defined as the ratio of the device temperature drop in the "on" state compared with the "off" state to the temperature difference between the device and environment in the "off" state. A larger η_1 value indicates a more significant temperature regulation capability of the flexible thermal switch. At different heat fluxes, the η_1 values of the flexible thermal switch remain stable at approximately 57.9%, and the detailed calculation process is provided in the Supporting Information. To assess the reversibility of the flexible thermal switch, four switching cycles were conducted. In each cycle, the heat flux was set to 600 W·m^{-2}, the environmental temperature was maintained at 26 °C, and the flexible thermal switch converted between "on" and "off" states. The device temperature at steady state in each cycle was recorded. The difference in T_d between the "on" and "off" states remained stable at approximately 4.3 °C across multiple cycles (Figure 4c), demonstrating reversible thermal conductivity regulation of the flexible thermal switch. In addition, as shown in Figure S7a, the thermal conductivity of the flexible thermal switch in the "off" state remains nearly unchanged after 100 on−off switching cycles, indicating good cycling stability.

Conventional thermal switches are generally restricted to planar devices, while the flexible thermal switch can also be applied to curved devices, effectively meeting diverse heat dissipation requirement. In practical applications, curved devices are relatively large and show differences in size. To meet this requirement, a Structure-A flexible thermal switch was further extended into a mesh construction, referred to as Structure-B (Figure 1b). Structure-B retains the same working principle as Structure-A but provides enhanced adaptability to curved heat sources, making it more suitable for practical thermal management scenarios. Therefore, the following results focus on Structure-B to evaluate its application performance. Taking a 4 × 6 grid as an example, the thermal conductivity is 0.283 W·m^{-1}·K^{-1} in the "off" state and 4.561 W·m^{-1}·K^{-1} in the "on" state, resulting in a thermal switching ratio of 16.1 (see Section S7.5 of the Supporting Information). Considering the geometric characteristics of curved monitors, foldable smartphones, and cylindrical batteries, the corresponding aluminum alloy structures were designed, as shown in Figure S9. A polyimide heating film was attached to one side of the aluminum alloy, a flexible thermal switch was placed on the other side, and thermocouples were positioned between the aluminum alloy and the heating film to monitor the heat source temperature. We assume that the working efficiency improves when the heat source temperature approaches 20 °C. The temperature deviation (ΔT) is defined as the deviation of the heat source temperature from the optimal temperature of 20 °C. Heat dissipation should be enhanced at high temperature and reduced at low temperature, thereby maintaining the heat source temperature as close to 20 °C as possible.

The heat source temperatures were measured at environmental temperatures (T_e) of 0 and 26 °C under three conditions: without a flexible thermal switch, with the flexible thermal switch in the "on" state, and with the flexible thermal switch in the "off" state, as shown in Figure 4d−f. At T_e = 26 °C, the heat source temperatures without flexible thermal switch and with it in the "on" state were nearly identical, both indicating effective heat dissipation. The temperature distribution of the heat source showed that the flexible thermal switch in the "on" state effectively reduced the heat source temperature compared with that in the "off" state. Conversely, at T_e = 0 °C, the highest heat source temperature was observed when the flexible thermal switch was in the "off" state, demonstrating its excellent thermal insulation capability. Under conditions with a low heat load or low environmental temperature, the flexible thermal switch remained in the "off" state to reduce heat loss. By contrast, under high heat load conditions, the flexible thermal switch was in the "on" state to enhance heat dissipation. Hence, the device temperature could be maintained within a suitable range by adjusting the magnetic induction intensity to change the thermal conductivity. With a flexible thermal switch, the temperature deviation can be reduced by 7.6% for a curved monitor, 10.2% for a foldable smartphone, and 4.9% for a cylindrical battery. The flexible thermal switch shows great potential for smart thermal management in curved or flexible systems, including curved monitors, foldable smartphones, cylindrical batteries, wearable devices, and soft robots. However, further advances in durability and magnetic actuation integration are still required before the flexible thermal switch can be practically implemented in real devices.

3. CONCLUSIONS

A flexible thermal switch consisting of magnetic liquid metal, graphene films, and PDMS was developed, and a continuous and reversible regulation of its thermal conductivity under a magnetic field was achieved. Under a magnetic field, magnetic liquid metal contacted the graphene film, forming a heat conduction pathway and switching the flexible thermal switch to the "on" state. In the absence of a magnetic field, magnetic liquid metal disconnected the heat conduction pathway due to gravity, and the flexible thermal switch reverted to the "off" state. Magnetic field can regulate the heat conduction pathway formed by magnetic liquid metal, so that thermal conductivity continuously varies between 0.261 and 3.426 W·m^{-1}·K^{-1}. The thermal switching ratio reaches 13.1, which is significantly higher than that of other thermal switches based on noncontact regulation mechanisms. The excellent temperature regulation ability of the flexible thermal switch was demonstrated through experiments. At different heat flux densities, the temperature difference between device and environment in the "on" state is reduced by approximately 57.9% compared with that in the "off" state. Furthermore, it reduces the temperature deviation of a foldable smartphone heat source by 10.2%. The flexible thermal switch provides smart thermal management for planar and curved devices, offering new perspectives for advanced thermal management in flexible electronic devices, soft robotics, and power batteries.

https://doi.org/10.1021/acsami.5c25437
ACS Appl. Mater. Interfaces 2026, 18, 15345−15354

4. EXPERIMENTAL SECTION

4.1. Preparation of Magnetic Liquid Metal (Figure 2a)

First, 40 g of EGaIn (75.5 wt % Ga and 24.5 wt % In) and 10 g of iron powder (particle size: 38 μm) were weighed and added into a beaker. Then, 5 mL of hydrochloric acid (20.0 wt % HCl) was added. The mixture was stirred at room temperature for approximately 3 min, during which the solution changed from turbid to transparent, indicating the successful dissolution of iron powder in EGaIn. A magnet was used to enrich the magnetic liquid metal, and the remaining hydrochloric acid solution was poured off. Finally, magnetic liquid metal with an iron powder mass fraction of 20% was obtained.

4.2. Preparation of PDMS Skeleton Structure

The PDMS is Sylgard 184 silicone elastomer, which consists of a prepolymer base and a cross-linking curing agent. The base and curing agent were mixed at a mass ratio of 10:1 and stirred for 10 min. The mixture was degassed in a vacuum oven for 20 min to remove bubbles. After degassing, the PDMS was poured into a mold and cured in a vacuum oven at 100 °C for 2 h. The cured PDMS was then demolded to obtain the PDMS skeleton.

4.3. Preparation of the Structure-A Flexible Thermal Switch (Figure 1a)

A PDMS skeleton structure with a side length of 25.5 mm and a thickness of 3.5 mm was prepared. The skeleton consisted of a rectangular cavity (21.1 × 21.1 × 2.0 mm^3) and a cylindrical cavity (18.0 mm diameter and 1.5 mm in thickness). These two cavities together constituted the internal space of the PDMS skeleton. The rectangular cavity was filled with magnetic liquid metal, while the cylindrical cavity was filled with air. Graphene films with a thickness of 0.1 mm were used as the upper and lower encapsulating layers of the flexible thermal switch. Due to the low surface energy of PDMS, direct bonding is difficult; therefore, the PDMS surface was treated with an adhesion promoter (770 primer). Subsequently, the PDMS skeleton and the graphene films were bonded using an ethyl cyanoacrylate instant adhesive.

4.4. Preparation of the Structure-B Flexible Thermal Switch (Figure 1b)

The PDMS skeleton consisted of a rectangular cavity and multiple grids with a width of 1.5 mm. These grids and the rectangular cavity together formed the internal cavity of the PDMS skeleton. The total thickness of the PDMS skeleton was 2.5 mm, resulting from the combination of the 1.0 mm grids and the 1.5 mm rectangular cavity. The rectangular cavity was filled with magnetic liquid metal, and the grid regions were filled with air. Both the top and bottom surfaces of the structure were encapsulated with graphene films of 0.1 mm thickness.

4.5. Characterization

The thermal conductivity of magnetic liquid metal was measured using the transient plane source method (Hot Disk TPS 2500 S). The hysteresis loop of the magnetic liquid metal was analyzed using a vibrating sample magnetometer measurement system (LakeShore 7404). The magnetic induction intensities at different distances from the magnet was measured using a Gaussmeter. The microstructure of the magnetic liquid metal was observed using SEM (QUANTA FEG 250). The heat conduction pathways under varying magnetic induction intensities were captured by using a high-speed camera (FASTCAM Mini UX 50). The thermal conductivity of the flexible thermal switch was evaluated using the steady-state method (Longwin LW-9389MD). Temperature was monitored by using a K-type thermocouple during experiments. Temperature distribution maps were captured by using an infrared thermal imager (Fotric 288+).

■ ASSOCIATED CONTENT

Supporting Information

The Supporting Information is available free of charge at https://pubs.acs.org/doi/10.1021/acsami.5c25437.

Performance comparison of thermal switches; surface morphology and capillary motion of magnetic liquid metal; thermal conductivity and thermal resistance analysis; finite element simulations; and cycling stability and smart thermal management (PDF)

Onset of magnetic liquid metal motion in a capillary tube under an applied magnetic field (MP4)

Reversible morphological evolution of magnetic liquid metal with and without a magnetic field (MP4)

■ AUTHOR INFORMATION

Corresponding Authors

Xudong Zhang − *State Key Laboratory of Cryogenic Science and Technology, Technical Institute of Physics and Chemistry, Chinese Academy of Sciences, Beijing 100190, China; School of Future Technology, University of Chinese Academy of Sciences, Beijing 100049, China*; Email: xdzhang@mail.ipc.ac.cn

Bingyang Cao − *Key Laboratory for Thermal Science and Power Engineering of Ministry of Education, Department of Engineering Mechanics, Tsinghua University, Beijing 100084, China*; orcid.org/0000-0003-3588-972X; Email: caoby@tsinghua.edu.cn

Authors

Yuxia Dong − *Key Laboratory for Thermal Science and Power Engineering of Ministry of Education, Department of Engineering Mechanics, Tsinghua University, Beijing 100084, China*

Bin Li − *Key Laboratory for Thermal Science and Power Engineering of Ministry of Education, Department of Engineering Mechanics, Tsinghua University, Beijing 100084, China*

Guanghao Sang − *State Key Laboratory of Cryogenic Science and Technology, Technical Institute of Physics and Chemistry, Chinese Academy of Sciences, Beijing 100190, China; School of Future Technology, University of Chinese Academy of Sciences, Beijing 100049, China*

Complete contact information is available at: https://pubs.acs.org/10.1021/acsami.5c25437

Notes

The authors declare no competing financial interest.

■ ACKNOWLEDGMENTS

This work was supported by the National Natural Science Foundation of China (Grant Nos. 52425601, 52327809, 52206098, and 82361138571), the National Key Research and Development Program of China (Grant No. 2023YFB4404104), and Beijing Natural Science Foundation (No. L233022).

■ REFERENCES

(1) Henry, A.; Prasher, R.; Majumdar, A. Five thermal energy grand challenges for decarbonization. *Nat. Energy* **2020**, *5* (9), 635−637.

(2) Koenders, S.; Loonen, R.; Hensen, J. Investigating the potential of a closed-loop dynamic insulation system for opaque building elements. *Energy Build.* **2018**, *173*, 409−427.
(3) Cui, Y.; Qin, Z.; Wu, H.; Li, M.; Hu, Y. Flexible thermal interface based on self-assembled boron arsenide for high-performance thermal management. *Nat. Commun.* **2021**, *12* (1), 1284.
(4) Jia, J.; Li, S.; Chen, X.; Shigesato, Y. Emerging Solid−State Thermal Switching Materials. *Adv. Funct. Mater.* **2024**, *34* (42), 2406667.
(5) Menyhart, K.; Krarti, M. Potential energy savings from deployment of Dynamic Insulation Materials for US residential buildings. *Build. Environ.* **2017**, *114*, 203−218.
(6) Moore, A. L.; Shi, L. Emerging challenges and materials for thermal management of electronics. *Mater. Today* **2014**, *17* (4), 163−174.
(7) Wang, J.; Feng, X.; Yu, Y.; Huang, H.; Zheng, M.; Xu, Y.; Wu, J.; Yang, Y.; Lu, J. Rapid temperature-responsive thermal regulator for safety management of battery modules. *Nat. Energy* **2024**, *9* (8), 939−946.
(8) Hengeveld, D. W.; Mathison, M. M.; Braun, J. E.; Groll, E. A.; Williams, A. D. Review of modern spacecraft thermal control technologies. *HVAC&R Res.* **2010**, *16* (2), 189−220.
(9) Zhang, H.; He, Q.; Zhang, F.; Duan, Y.; Qin, M.; Feng, W. Biomimetic Intelligent Thermal Management Materials: From Nature-Inspired Design to Machine-Learning-Driven Discovery. *Adv. Mater.* **2025**, *37*, 2503140.
(10) Li, Y.; Li, W.; Han, T.; Zheng, X.; Li, J.; Li, B.; Fan, S.; Qiu, C.-W. Transforming heat transfer with thermal metamaterials and devices. *Nat. Rev. Mater.* **2021**, *6* (6), 488−507.
(11) Xie, R.; Bui, C. T.; Varghese, B.; Zhang, Q.; Sow, C. H.; Li, B.; Thong, J. T. An Electrically Tuned Solid-State Thermal Memory Based on Metal−Insulator Transition of Single-Crystalline VO_2 Nanobeams. *Adv. Funct. Mater.* **2011**, *21* (9), 1602−1607.
(12) Wehmeyer, G.; Yabuki, T.; Monachon, C.; Wu, J.; Dames, C. Thermal diodes, regulators, and switches: Physical mechanisms and potential applications. *Appl. Phys. Rev.* **2017**, *4* (4), 041304.
(13) Zhang, Z.; Cao, B. Thermal smart materials with tunable thermal conductivity: Mechanisms, materials, and applications. *Sci. China Phys. Mech. Astron.* **2022**, *65* (11), 117003.
(14) Deng, S.; Yuan, J.; Lin, Y.; Yu, X.; Ma, D.; Huang, Y.; Ji, R.; Zhang, G.; Yang, N. Electric-field-induced modulation of thermal conductivity in poly (vinylidene fluoride). *Nano Energy* **2021**, *82*, 105749.
(15) Zhang, Z.-T.; Dong, Y.-X.; Cao, B.-Y. Promoting temperature control and energy conservation by smart thermal management using nanoparticle suspensions with tunable thermal conductivity. *Appl. Energy* **2024**, *374*, 124097.
(16) Andrade, V. M.; Fernandes, C. R.; Teixeira, J. S.; Pereira, C.; Pires, A. L.; Silva, D. J.; Ventura, J.; Oliveira, J. High-performance magnetic thermal switch based on $MnFe_2O_4$/Ethylene Glycol: Water refrigerant dispersion. *Energy* **2023**, *283*, 129123.
(17) Philip, J.; Shima, P.; Raj, B. Nanofluid with tunable thermal properties. *Appl. Phys. Lett.* **2008**, *92* (4), 043108.
(18) Sun, P.; Huang, Y.; Zheng, R.; Cheng, G.; Wan, Q.; Ding, Y. Magnetic graphite suspensions with reversible thermal conductivity. *Mater. Lett.* **2015**, *149*, 92−94.
(19) Shin, J.; Sung, J.; Kang, M.; Xie, X.; Lee, B.; Lee, K. M.; White, T. J.; Leal, C.; Sottos, N. R.; Braun, P. V.; et al. Light-triggered thermal conductivity switching in azobenzene polymers. *Proc. Natl. Acad. Sci. U.S.A.* **2019**, *116* (13), 5973−5978.
(20) Zheng, Q.; Murray, S. E.; Diao, Z.; Bhutani, A.; Shoemaker, D. P.; Cahill, D. G. Thermal transport through the magnetic martensitic transition in Mn_xMGe (M = Co, Ni). *Phys. Rev. Mater.* **2018**, *2* (7), 075401.
(21) Sun, P.; Wu, Y.; Gao, J.; Cheng, G.; Chen, G.; Zheng, R. Room temperature electrical and thermal switching CNT/hexadecane composites. *Adv. Mater.* **2013**, *25* (35), 4938−4943.
(22) Zheng, R.; Gao, J.; Wang, J.; Chen, G. Reversible temperature regulation of electrical and thermal conductivity using liquid−solid phase transitions. *Nat. Commun.* **2011**, *2* (1), 289.
(23) Du, T.; Xiong, Z.; Delgado, L.; Liao, W.; Peoples, J.; Kantharaj, R.; Chowdhury, P. R.; Marconnet, A.; Ruan, X. Wide range continuously tunable and fast thermal switching based on compressible graphene composite foams. *Nat. Commun.* **2021**, *12* (1), 4915.
(24) Yu, D.; Liao, Y.; Song, Y.; Wang, S.; Wan, H.; Zeng, Y.; Yin, T.; Yang, W.; He, Z. A Super-Stretchable Liquid Metal Foamed Elastomer for Tunable Control of Electromagnetic Waves and Thermal Transport. *Adv. Sci.* **2020**, *7* (12), 2000177.
(25) Li, J.; Zhou, Y.; Jiang, C.; Lei, D.; Yu, X. Recent advances in passive cooling materials for thermal management in flexible electronics. *J. Mater. Chem. C* **2024**, *12* (32), 12179−12206.
(26) Zhang, Y.; Li, P.; Quan, J.; Li, L.; Zhang, G.; Zhou, D. Progress, challenges, and prospects of soft robotics for space applications. *Adv. Intell. Syst.* **2023**, *5* (3), 2200071.
(27) Yun, J.; Yoo, Y. J.; Kim, H. R.; Song, Y. M. Recent progress in thermal management for flexible/wearable devices. *Soft Sci.* **2023**, *3*, 12.
(28) Cui, J.; Xu, W.; Yu, Q.; Ma, Y.; Hu, Z.; Zhang, C.; Xu, C.; Xu, Y.; Ling, W.; Zhou, W. Development of high-efficiency flexible heat pipe device for thermal management in foldable phones. *Energy* **2025**, *328*, 136545.
(29) Ahmadian-Elmi, M.; Zhao, P. Review of thermal management strategies for cylindrical lithium-ion battery packs. *Batteries* **2024**, *10* (2), 50.
(30) An, K.; Su, Z.; Zhang, M.; Deng, Y. Liquid metal-based micro/mini-channel heat transfer: Progress, challenges, and opportunities. *Appl. Therm. Eng.* **2024**, *250*, 123551.
(31) Zhang, X.-D.; Zhang, Z.-T.; Wang, H.-Z.; Cao, B.-Y. Thermal interface materials with high thermal conductivity and low young's modulus using a solid−liquid metal codoping strategy. *ACS Appl. Mater. Interfaces* **2023**, *15* (2), 3534−3542.
(32) Yao, B.; Xu, X.; Li, H.; Han, Z.; Hao, J.; Yang, G.; Xie, Z.; Chen, Y.; Liu, W.; Wang, Q.; et al. Soft liquid-metal/elastomer foam with compression-adjustable thermal conductivity and electromagnetic interference shielding. *Chem. Eng. J.* **2021**, *410*, 128288.
(33) Zhao, R.; Kang, S.; Wu, C.; Cheng, Z.; Xie, Z.; Liu, Y.; Zhang, D. Designable electrical/thermal coordinated dual-regulation based on liquid metal shape memory polymer foam for smart switch. *Adv. Sci.* **2023**, *10* (8), 2205428.
(34) Luo, W.; Zhang, X.; Luo, T.; Li, B.; Wei, B.; Zhang, J.; Zhu, G. A Flexible Thermal Interface Material as the Heat Switch for Solid-State Cooling. *Adv. Funct. Mater.* **2026**, *36*, No. e12421.
(35) Zhu, P.; Zhang, J.; Wei, B.; Li, B.; Zhu, G. Liquid metal enabled thermal switch for active thermal management. *Int. J. Heat Mass Transfer* **2026**, *254*, 127654.
(36) Kim, D.; Jeong, J.; Chung, S. K.; Lee, J. B. Magnetic liquid metals: a review. *Adv. Funct. Mater.* **2024**, *34* (31), 2311153.
(37) Hu, L.; Wang, H.; Wang, X.; Liu, X.; Guo, J.; Liu, J. Magnetic liquid metals manipulated in the three-dimensional free space. *ACS Appl. Mater. Interfaces* **2019**, *11* (8), 8685−8692.
(38) Liu, M.; Wang, Y.; Kuai, Y.; Cong, J.; Xu, Y.; Piao, H. G.; Pan, L.; Liu, Y. Magnetically Powered Shape-Transformable Liquid Metal Micromotors. *Small* **2019**, *15* (52), 1905446.
(39) Tang, J.; Zhao, X.; Li, J.; Zhou, Y.; Liu, J. Liquid metal phagocytosis: intermetallic wetting induced particle internalization. *Adv. Sci.* **2017**, *4* (5), 1700024.
(40) Wang, H.; Chen, S.; Li, H.; Chen, X.; Cheng, J.; Shao, Y.; Zhang, C.; Zhang, J.; Fan, L.; Chang, H.; et al. A liquid gripper based on phase transitional metallic ferrofluid. *Adv. Funct. Mater.* **2021**, *31* (32), 2100274.
(41) Zhang, Y.; Jiang, S.; Hu, Y.; Wu, T.; Zhang, Y.; Li, H.; Li, A.; Zhang, Y.; Wu, H.; Ding, Y.; et al. Reconfigurable magnetic liquid metal robot for high-performance droplet manipulation. *Nano Lett.* **2022**, *22* (7), 2923−2933.

https://doi.org/10.1021/acsami.5c25437
ACS Appl. Mater. Interfaces 2026, 18, 15345−15354

(42) Fu, H.; Gao, L. Theory for anisotropic thermal conductivity of magnetic nanofluids. *Phys. Lett. A* **2011**, *375* (41), 3588−3592.
(43) Nguyen, N.-T.; Zhu, G.; Chua, Y.-C.; Phan, V.-N.; Tan, S.-H. Magnetowetting and sliding motion of a sessile ferrofluid droplet in the presence of a permanent magnet. *Langmuir* **2010**, *26* (15), 12553−12559.
(44) He, X.; Ni, M.; Wu, J.; Xuan, S.; Gong, X. Hard-magnetic liquid metal droplets with excellent magnetic field dependent mobility and elasticity. *J. Mater. Sci. Technol.* **2021**, *92*, 60−68.
(45) Stevar, M.; Vorobev, A. Shapes and dynamics of miscible liquid/liquid interfaces in horizontal capillary tubes. *J. Colloid Interface Sci.* **2012**, *383* (1), 184−197.

https://doi.org/10.1021/acsami.5c25437
ACS Appl. Mater. Interfaces 2026, 18, 15345−15354